



Critical assessment of Co-Cu phase diagram from first-principles calculationsChangle Li ^{1,*} Henrik Levämäki ¹ Ruiwen Xie,¹ Liyun Tian,² Zhihua Dong,¹ Wei Li,² Song Lu,^{1,†} Qing Chen,³ John Ågren,⁴ and Levente Vitos ^{1,2,5}¹*Applied Materials Physics, Department of Materials Science and Engineering, KTH Royal Institute of Technology, Stockholm SE-10044, Sweden*²*Department of Physics and Astronomy, Division of Materials Theory, Uppsala University, Box 516, SE-75120 Uppsala, Sweden*³*Thermo-Calc Software AB, Råsundavägen 18, SE-16967 Solna, Sweden*⁴*Department of Materials Science and Engineering, Division of Physical Metallurgy, KTH Royal Institute of Technology, Stockholm SE-10044, Sweden*⁵*Research Institute for Solid State Physics and Optics, Wigner Research Center for Physics, Budapest H-1525, Hungary*

(Received 4 June 2020; accepted 6 November 2020; published 24 November 2020)

Using first-principles alloy theory, we perform a systematic study of the Co-Cu phase diagram. Calculations are carried out for ferromagnetic and paramagnetic $\text{Co}_{1-x}\text{Cu}_x$ solid solutions with face-centered-cubic (fcc) crystal structure. We find that the equilibrium volumes and magnetic states are crucial for a quantitative description of the thermodynamics of the Co-Cu system at temperatures up to 1400 K. In particular, the paramagnetic state of Cu-rich alloys with persisting local magnetic moments is shown to be responsible for the solubility of a small amount of Co in fcc Cu whereas the excess entropy in the ferromagnetic Co-rich region critically depends on the adopted lattice parameters. None of the common local or semilocal density functional theory approximations have the necessary accuracy for the lattice parameters when compared to the experimental data. The predicted *ab initio* Co-Cu phase diagram is in good agreement with the measurements and CALPHAD data, making it possible to gain a deep insight into the various contributions to the Gibbs free energy. The present study provides an atomic-level description of the thermodynamic quantities controlling the limited mutual solubility of Co and Cu and highlights the importance of high-temperature magnetism.

DOI: [10.1103/PhysRevB.102.184428](https://doi.org/10.1103/PhysRevB.102.184428)**I. INTRODUCTION**

A fundamental factor in applying first-principles methods to material design is the accurate description of the thermo-mechanics [1–3]. Although computations based on density functional theory (DFT) have been widely used to calculate properties such as equilibrium volume, elastic moduli, and formation enthalpy at static (0 K) state [4–7], using first-principles methods to capture high-temperature properties of materials is very challenging [8]. That is primarily due to the difficulties in the descriptions of various types of excitations including phonons and magnons. Therefore, first-principles calculations are often used to establish the equilibrium phase diagram at static condition via the calculations of the phase stability for various structures or phases. Such calculations provide important information missing in the experimental phase diagrams at the low-temperature part. Beyond experiments, phase diagrams are often calculated by

computational thermodynamics, e.g., CALPHAD (CALCulation of PHase Diagrams) [9,10], a semiempirical method to compute multicomponent phase diagrams by modeling the Gibbs free energy of individual phases with model parameters fitted to the experimental data on phase equilibrium and thermochemical properties of binary and ternary systems. We notice that Miedema's model has also been used to estimate the heat of mixing of binary solution phases over their whole composition ranges when no experimental data was available [11,12]. Tools based on the thermodynamic approach, such as Thermo-Calc [13–15], are able to predict the thermodynamic properties of alloys with acceptable accuracy providing that reliable experimental data has been taken into account in the development of the database [16,17]. There are recent efforts to include *ab initio* results into the database for CALPHAD calculations [18–21], aiming at enhancing the predicting power of these methods at low temperatures. Therefore, a direct comparison of the thermodynamic properties derived from first-principles and Thermo-Calc approaches provides insight into the atomistic mechanisms behind the observed behavior and ensures the high accuracy for efficient material design.

The Co-Cu alloys, as an important system for the production of electrothermal materials, have been widely studied in experiments and theoretical modelings [22–28]. The calculated phase diagram of Co-Cu, shown in Fig. 1, exhibits magnetic and structural phase transitions as a function of concentration. It is apparent that Co and Cu become miscible

*changle@kth.se

†songlu@kth.se

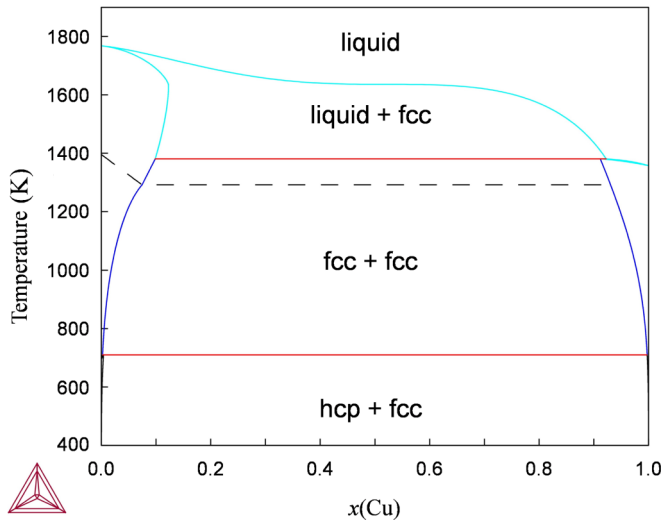


FIG. 1. Calculated phase diagram for Co-Cu system using the Thermo-Calc software. These thermodynamic data were exclusively derived from experimental data over the entire composition range [24]. The dashed line is the experimental Curie temperature.

in each other only at elevated temperature, with almost 100% miscibility gap below 800 K. In pure Co, a phase transition from hexagonal close-packed (hcp) to face-centered cubic (fcc) phase occurs at 695 K [29]. Since Co remains ferromagnetic up to ~ 1400 K, the proper description of the magnetic state for fcc Co-Cu alloys is essential for accurate free energies at elevated temperatures. In recent years, the magnetic properties of the Co-Cu system attracted some interest. Mashimo *et al.* [30] studied the magnetic properties of Co-Cu alloys prepared by mechanical alloying and found that the Co-rich region is ferromagnetic, while the Cu-rich region is paramagnetic at room temperature. It is clear that one should pay special attention to the role of magnetism when discussing the energetics of the Co-Cu binary system.

The purpose of this work is to assess the phase diagram of the Co-Cu binary system from first-principles quantum mechanical calculations. To this end, we compute the thermophysical parameters of the fcc Co-Cu alloys in order to estimate the thermodynamic stability at temperatures between 0–1400 K. In practice, we establish all important terms in the Gibbs free energy using our *ab initio* thermophysical parameters. In accordance with the experimental [30] and the present theoretical magnetic phase diagrams, we consider ferromagnetic (FM) state in the Co-rich region and paramagnetic (PM) state in the Cu-rich region. The theoretical *ab initio* phase diagram is compared to the one obtained by Thermo-Calc. The impact of the individual terms is discussed. The present theoretical results give a solid basis for the thermodynamics of the Co-Cu system and emphasize the importance of magnetism at elevated temperatures. Furthermore, we point out that highly accurate equations of state for the alloys and end members are required for a quantitative description of the entropy especially in the Co-rich region. The rest of the paper is arranged as follows. We present the computational details and methodologies for calculating thermophysical properties in Sec. II. The obtained lattice parameters, Curie temperature,

and elastic properties are presented in Secs. III A, III B, and III C. The results for the enthalpy, entropy, and free energy are introduced and discussed in Secs. III D, III E, and III F. Finally, the main findings and conclusions are summarized in Sec. IV.

II. METHODOLOGY

A. Total energy method

The total-energy calculations were performed using density functional theory (DFT) [31] as formulated in the exact muffin-tin orbitals (EMTO) method [32], using the Green function and full charge density techniques. The self-consistent calculations were carried out based on the generalized gradient approximation via the Perdew-Burke-Ernzerhof (PBE) [33] approximation and the quasi-non-uniform approximation (QNA) [34–36] for describing the exchange-correlation interactions. Alternative approximations such as PBEsol [37] and AM05 [38] were also tested, but since the results are similar to those obtained by the PBE and QNA approximations those results are not explicitly shown here. We adopted the coherent potential approximation (CPA) [39,40] to describe the compositional and magnetic disorder. The magnetic disorder in the PM state was accounted for by using the disordered local moment (DLM) model [41]. The EMTO method formulates an efficient and accurate approach for solving the Kohn-Sham equations [42,43]. By using large overlapping potential spheres, it describes more accurately the exact crystal potential compared with the conventional muffin-tin or nonoverlapping approaches [44,45]. The EMTO method has been successfully applied in a number of first-principles calculations of the ground state properties of alloys [46–48]. In addition to the EMTO-CPA calculations, we also carried out supercell calculations where we went beyond the single-site CPA and could take into account the local lattice relaxation and chemical ordering effects. In the supercell calculations, we employed the special quasirandom structure (SQS) approach [49,50] in combination with the grid-based projector augmented-wave (GPAW) code [51–53] and the PBE approximation.

B. Thermodynamic modeling

The CALPHAD calculation was performed by using Thermo-Calc version 2020b and the accompanying free database TCBIN [15], which includes the thermodynamic description of the Co-Cu system from Kubistal and Vrestal [24]. Thermo-Calc provides a user friendly graphic interface and users can access the TCBIN database via the BINARY module. After selecting the elements Co and Cu, users can choose to calculate either the phase diagram of the Co-Cu system or the thermodynamic properties of any phase at any temperature in this binary system. The calculation results are automatically shown as graphs and can be tabulated.

C. Elastic properties

In a cubic lattice, there are three independent single-crystal elastic constants, c_{11} , c_{12} , and c_{44} . Usually, c_{11} and c_{12} are derived from the bulk modulus $B = (c_{11} + 2c_{12})/3$

and the tetragonal shear modulus $c' = (c_{11} - c_{12})/2$. In the present case, the bulk modulus (B) was calculated as a function of Wigner-Seitz radius (w) using the Morse function fitted to the total energies computed as a function of volume per atom, $V = 4\pi w^3/3$. The two cubic shear elastic constants c' and c_{44} were computed as a function of Wigner-Seitz radius using orthorhombic and monoclinic distortions as described in Ref. [43]. On a large scale, polycrystalline materials can be considered as quasi-isotropic or isotropic and an isotropic system is completely described by B and the shear modulus G . Here, we adopted the arithmetic Hill average to obtain the polycrystalline shear modulus, viz., $G = (G_R + G_V)/2$, where the Reuss and Voigt bounds are given by $G_R = 5(c_{11} - c_{12})c_{44}(4c_{44} + 3c_{11} - 3c_{12})^{-1}$ and $G_V = (c_{11} - c_{12} + 3c_{44})/5$, respectively. The Young modulus (E) and Poisson ratio (ν) are connected to B and G by the relations $E = 9BG/(3B + G)$ and $\nu = (3B - 2G)/(6B + 2G)$. The average sound velocity is given by $3v_m^{-3} = v_L^{-3} + 2v_T^{-3}$, where the longitudinal velocity is $\rho v_L^2 = B + 4G/3$ and the transversal velocity is $\rho v_T^2 = G$ with ρ being the average density. The Debye temperature (Θ) for a polycrystalline material is described as $\Theta = h/(2\pi k_B)(6\pi^2/V)^{1/3}v_m$, where h and k_B are the Planck and Boltzmann constants, respectively [54,55]. In the above expression, both the mean sound velocity and the volume V are temperature dependent. For the temperature dependence, we adopted the quasiharmonic approximation. Namely we computed all elastic parameters including the Debye temperature as a function of volume and connected the volume to temperature via the thermal expansion. The thermal expansion coefficient for different concentrations in turn was estimated by a linear relationship based on the experimental thermal expansion coefficients of pure Co and pure Cu [56].

D. Gibbs free energy

The Gibbs free energy $G(x, T)$ is expressed as a function of concentration (x) and temperature (T) using the following approximation

$$G(x, T) = E_{\text{int}}(x, T) - T[S_{\text{conf}}(x) + S_{\text{vib}}(x, T) + S_{\text{mag}}(x, T)] + E_{\text{vib}}(x, T) + \Delta F_{\text{ele}}(x, T). \quad (1)$$

Here E_{int} is the internal energy calculated for concentration x and volume corresponding to temperature T ; S_{conf} , S_{vib} , and S_{mag} are the entropy contribution due to the configurational, vibrational, and magnetic degrees of freedom, respectively. According to, e.g., Refs. [8,54,57], the vibrational energy $E_{\text{vib}}(x, T) = 9/8k_B\Theta + 3k_BTD(\Theta/T)$, where the Debye function is $D(x) = 3/x^3 \int_0^x t^3/(e^t - 1) dt$. $\Delta F_{\text{ele}} = F_{\text{ele}} - E_{\text{int}}$ is the free energy contribution due to finite temperature electronic excitations, where F_{ele} is the internal energy computed with the Fermi-Dirac distribution. All energy and entropy terms are expressed per atom.

The configurational and magnetic entropies are computed within the mean-field approximation, namely, $S_{\text{conf}} = -k_B \sum x_i \ln(x_i)$, where x_i is the concentration of alloy components (in our case $x_1 = x$ and $x_2 = 1 - x$), $S_{\text{mag}} = -k_B \sum x_i \ln(1 + \mu_i)$, where μ_i is the local magnetic moment of alloy component i calculated for the corresponding volume. The local magnetic moment is expressed in Bohr magneton. Magnetic entropy was taken into account for the PM state,

whereas for the FM state it was assumed to be zero. Obviously, neglecting the magnetic excitations in the FM state especially close to the Curie point introduces some errors in the Gibbs energy due to the missing magnetic free energy contribution. This error is expected to be the largest near the solubility limit around 1400 K. The vibrational entropy is computed from the temperature dependent Debye temperature using the expression $S_{\text{vib}} = 3k_B\{4/3D(\Theta/T) - \ln[1 - \exp(-\Theta/T)]\}$, which reduces to $S_{\text{vib}} = k_B[4 + 3\ln(T/\Theta)]$ in the high-temperature limit (see Ref. [41]). We notice that Co and Cu are miscible in each other only at elevated temperatures (see Fig. 1) where such a high temperature expression holds to a very good approximation.

E. Computational details

The EMTO Green function was calculated for 16 complex energy points distributed exponentially on a semicircular contour including the valence states. In the basis set we included s , p , d , and f orbitals ($l_{\text{max}} = 4$), and for the full charge density we used the l cutoff $l_{\text{max}}^h = 8$. The electrostatic correction to the single-site approximation was described using the screened impurity model with a screening parameter of 0.6 [58]. To ensure the numerical accuracy the integration over the Brillouin zone was done using a $37 \times 37 \times 37$ uniform grid of k points for equation of state calculations, whereas it was increased to $45 \times 45 \times 45$ for the calculations of the elastic constants. The Co-rich alloys were described in the FM state at temperatures ranging between 0 K and 1400 K (that is below the Curie temperature of Co, $T_C^{\text{Co}} = 1394$ K). According to the experimental phase diagram of Co-Cu alloys [23,29,59], we simulated the Cu-rich alloys within the PM state using the DLM scheme. We should recall that Co at temperatures below 695 K has the hcp structure, which is not considered here due to the very small solubility of Cu in hcp Co. We mention, however, that the hcp-fcc phase transition in Co was recently successfully described using *ab initio* tools by Lizarraga *et al.* [60].

In the GPAW-SQS calculations, we used a 32-atom unit cell, which was constructed from eight primitive fcc unit cells in $2 \times 2 \times 2$ shape [61]. The k -point mesh was set as $8 \times 8 \times 8$ using the Monkhorst-Pack scheme [62]. The plane-wave expansion cutoff energy was adopted to 700 eV and the relaxations were deemed finished when all forces and stresses were below 0.05 eV/Å. For the Brillouin zone integration, we used Fermi-Dirac statistics and the smearing width was chosen to be 0.01 eV. Short-range order calculations were performed by generating a set of 32-atom structures with varying degree of short-range order, which was quantified by the Warren-Cowley short-range order parameters α_i [63]. The structures were generated using the methodology presented in Ref. [64].

III. RESULTS AND DISCUSSION

A. Lattice parameter

For pure Co and Cu, the EMTO method has the accuracy of the most accurate full-potential methods [35,60]. For fcc $\text{Co}_{1-x}\text{Cu}_x$ random alloys, a careful survey of the available experimental data for the equilibrium lattice parameter is

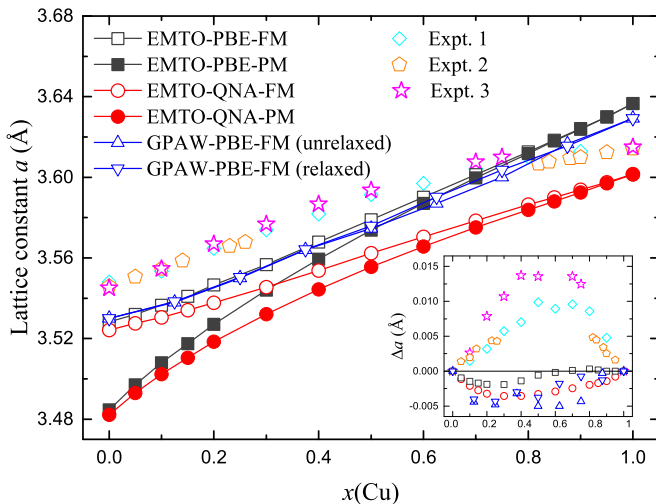


FIG. 2. The calculated lattice constants of fcc Co-Cu random alloys as a function of Cu concentration (x) for ferromagnetic (FM, open symbols) and paramagnetic (PM, solid symbols) states. The EMTO calculations were done using the PBE (square symbols) and QNA (circle symbols) exchange-correlation approximation. The GPAW results (triangle symbols) with and without lattice relaxation were obtained using the PBE approximation. Three sets of experimental data (Refs. [23,29,30]) are plotted for comparison. The deviations from Vegard's law for all calculated results in the FM state and all experimental data are plotted together in the inset figure. Note that all theoretical lattice constants are computed at static conditions and the experimental data are measured at room temperature.

collected in Fig. 2 [23,29,30]. The present EMTO (PBE and QNA) results for the equilibrium (static conditions) lattice constants obtained for the FM and PM states are also plotted, as well as the GPAW-PBE results with and without lattice relaxation. For a more quantitative comparison, in the inset of Fig. 2 we show the deviations relative to Vegard's law as a function of x .

For both FM and PM states, the PBE lattice parameters show a significantly larger slope as a function of Cu content compared to the experimental data. This is primarily due to the fact that PBE underestimates (overestimates) the equilibrium volume of Co (Cu), which is a well-known effect [35,65]. For the FM state, the QNA lattice constants are in line with Vegard's law. Recalling the fact that QNA by construction is practically exact for pure elements, the nearly composition independent shift relative to the linear rule of mixture can be ascribed to the neglected thermal effects. For Cu, the FM and PM results agree with each other (both of them correspond to the nonmagnetic solution). For Co, the PM volume is much smaller than the FM one, which is due to the loss of the magnetic pressure present primarily in the FM state. As a result, the lattice constants in the PM state have a clear negative curvature as a function of Cu concentration. We observe that the experimental lattice constants show a significant positive deviation compared to the Vegard's line. Indeed, the $\Delta a(x) = a(x) - x \times a(\text{Cu}) - (1-x) \times a(\text{Co})$ data plotted in the inset show that all experimental lattice constants deviate strongly from the linear behavior, while the theoretical (FM) results are rather close to a linear trend. Comparing the PBE

and QNA values, we find that the QNA lattice constants have a better agreement with the experimental data in line with Refs. [63,66]. We recall that the theoretical results in Fig. 2 correspond to static conditions whereas the experimental data to room-temperature and thus smaller theoretical values are expected for all concentrations. It should be noted that the EMTO results are very close to GPAW values obtained for the FM state and PBE approximation.

As we have seen, the present *ab initio* calculations are not able to reproduce the trend of the experimental lattice constants, especially the significant positive deviation compared to the Vegard's line. Exceptions are the results obtained for the PM state, but we completely rule out those data for the entire compositional interval since Co-rich alloys were found to be ferromagnetic [29]. The lack of the positive deviation in the theoretical results could potentially be caused by the single-site CPA, if either local relaxations or short ranged chemical ordering, or both, were an important factor. However, as Fig. 2 shows, both the relaxed and unrelaxed GPAW-PBE lattice constants exhibit weak positive curvature, so local relaxations do not seem to be the cause behind the observed deviation between theory and experiment. Furthermore, by comparing the unrelaxed supercell and CPA results, we find that the mean-field description of the solid solution as compared to the more precise supercell model does not introduce any substantial error either.

We have also investigated the possible impact of the short-range order by calculating a set of structures with varying degree of short-range order for $x = 0.5$ alloys. Short-range order in these structures was measured by the Warren-Cowley parameters α_i , which describe the pair correlation between different types of atoms on the i th nearest neighbor shell. The most important parameter is α_1 , which for fcc structure is zero for fully random structures and $-1/3$ for fully ordered $L1_0$ and $L1_2$ structures. Here we focus on the first three nearest neighbor shells and neglect the rest. In order to explore a range of different short-range order situations, we have calculated eight different structures in the range $-0.15 \leq \alpha_1 \leq 0$, where for one half α_2 and α_3 are decided by the minimum entropy condition (maximize $|\alpha_2|$ and $|\alpha_3|$) and for the other half by the maximum entropy condition (minimize $|\alpha_2|$ and $|\alpha_3|$) [63]. Local relaxations and cell optimization were taken into account in all of these supercell calculations. The result is that short-range order can positively increase the lattice constant of the alloys up to ~ 0.005 Å compared to Vegard's rule. This increase induced by local ordering effects explains about 30% of the positive deviation that is seen in the experimental data. Based on these findings, we conclude that the positive deviation relative to the linear trend observed in the experimental data cannot be captured by regular DFT calculations and effects beyond DFT, further thermal effects (thermomagnetic or long-range order effects), or alloy preparation could be behind this trend. In particular, we notice that mechanical alloying was reported to introduce a certain amount of N and O into the lattice which could eventually explain the observed substantial positive deviation in the lattice parameters relative to a linear trend [23]. As we will see later, this positive deviation from Vegard's law is critical for a quantitative description of the excess entropy and thus we call for further in-depth analysis to reveal the exact origin of this phenomenon. In the following

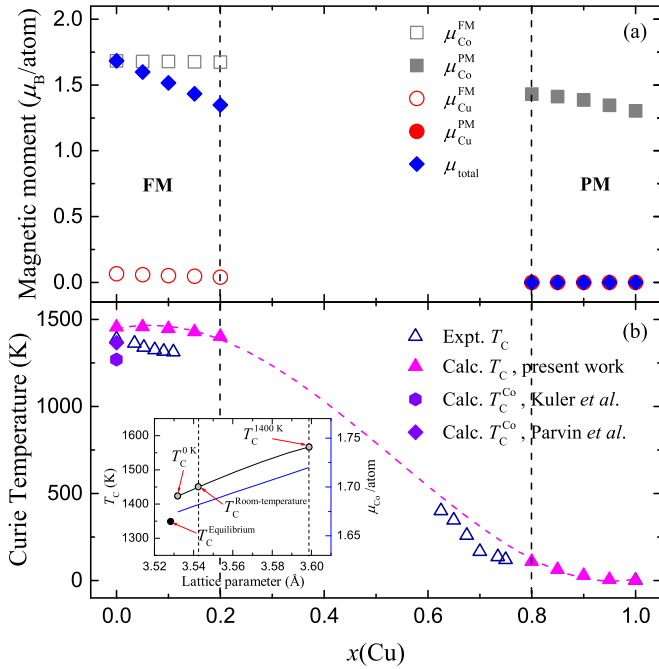


FIG. 3. The calculated magnetic moments and Curie temperature using the experimental volumes for Co-Cu random alloys in the Co-rich ($0 \leq x \leq 0.2$) and Cu-rich ($0.8 \leq x \leq 1$) regions. Panel (a) shows the calculated magnetic moments for Co (μ_{Co} , square symbols) and Cu (μ_{Cu} , circle symbols) for the FM (open symbols) and PM (solid symbols) states, as well as total magnetic moment (μ_{total} , blue symbols). Panel (b) presents the theoretical Curie temperature (T_C) for the fcc Co-Cu alloys calculated using the room-temperature volumes. For comparison, the experiment measured data (Ref. [70]) are also plotted, as well as two previous theoretical T_C values for Co (Refs. [67,71]). The inset in panel (b) shows the variations of the theoretical Curie temperature and magnetic moments (μ_{Co} , blue line) for pure Co with respect to the lattice parameters corresponding to temperatures from 0 K to 1400 K. The separate point around 3.528 Å ($T_C^{\text{Equilibrium}}$) is the result obtained using the theoretical equilibrium (static) total energies for both FM and PM states.

ab initio theoretical study, we will adopt the experimental lattice parameters [23] and use the thermal expansion to get the volume at each temperature. For comparison, we will also show results obtained adopting the static theoretical volume (and scaled with the thermal expansion coefficient to get the theoretical volume as a function of temperature) to highlight the importance of the correct volume used in the *ab initio* calculations. All remaining calculations will be carried out based on the PBE approximation for describing the exchange-correlation interactions.

B. Magnetic structure

In the Co-Cu binary system, the Co-rich region shows ferromagnetic order, while the Cu-rich region is paramagnetic with very low ordering temperature. We plot the variation of the total magnetic moments (μ_{total}) calculated using the experimental volumes for the FM and PM states in Fig. 3(a), together with the local moments for Co and Cu components. The present calculated magnetic moments of pure Co ($x = 0$) is 1.68 μ_B , which agrees well with the previous values

[30,67,68]. In the Co-rich region, the total magnetic moment gradually decreases with increasing Cu concentration. The local magnetic moments of Co and Cu remain basically stable with composition. In the Cu-rich side, the total magnetic moment is zero due to the PM state. However, even in the Cu-rich dilute PM alloys, the Co atoms possess sizable local magnetic moments. However, as we will see it below the coupling between these local Co moments is not strong enough to maintain a long-range magnetic order at finite temperatures. We notice that freezing the Co moments to zero (i.e., neglecting the spin polarization in the Cu-rich end of the phase diagram) increases the FM (PM) total energy of the system by 1.2–2.2 mRy/atom. These results were obtained by CPA which may not properly capture the physics of dilute magnetic moments. Because of that, we also checked the local magnetic moments in the FM state as predicted by CPA and SQS in the Cu-rich region. They turn out to be 1.50 μ_B and 1.54 μ_B , respectively, showing that the survival of the local magnetic moments on Co atoms embedded in a Cu matrix is not an artifact of the mean-field approximation.

We calculated the Curie temperature (T_C) for fcc Co-Cu alloys and compare it with the experimental data in Fig. 3(b). Here the Curie temperature was estimated using the mean-field approximation [69], $3k_B T_C = 2(E_{\text{tot}}^{\text{PM}} - E_{\text{tot}}^{\text{FM}})/(1 - x)$, where $(E_{\text{tot}}^{\text{PM}} - E_{\text{tot}}^{\text{FM}})$ is the difference between the total energies of the PM and FM states and x is the concentration of nonmagnetic element (Cu). For comparison, the experiment data [70] as well as previous theoretical results [67,71] are also shown in the figure. In the Co-rich region, the calculated T_C gradually decreased with increasing Cu concentration, whereas in the Cu-rich region T_C approaches 0 K. In general, the calculated T_C is in good agreement with the measurements. The present theoretical predictions for the magnetic ordering temperature fully support the magnetic phase diagram shown in Fig. 1 and give a theoretical support behind the FM and PM states employed for the Co-rich and Cu-rich regions, respectively. We notice that a more advanced spin dynamics modeling based on magnetic Hamiltonian (not shown) leads to very similar magnetic transition temperatures as those shown in Fig. 3(b).

We emphasize that the adopted lattice constant is important when estimating the Curie temperature since different volumes yield different mean-field T_C values. To illustrate this effect, in the inset of Fig. 3, we plot the calculated T_C and magnetic moments (μ_{Co}) for pure Co with respect to the lattice parameter. It is found that the calculated T_C and μ_{Co} increase as the lattice parameter used in the total energy calculations increases. We find that the larger local magnetic moment with increasing volume stabilizes the FM state with respect to the PM one which leads to the increase in the Curie temperature. The predicted T_C using the theoretical equilibrium volumes of the FM and PM states (corresponding to zero pressure in both magnetic states) is $T_C^{\text{Equilibrium}} = 1349$ K, which agrees well with previous mean-field results (1270 K [67] and 1360 K [71] for Co). The theoretical T_C for fcc Co using the room-temperature volume (for both the FM and PM states) is $T_C^{\text{Room-temperature}} = 1456$ K, which agrees reasonably well with the experimental Curie temperature of Co ($T_C = 1388$ K). We note that almost the same value ($T_C^{0\text{K}} = 1429$ K) is predicted

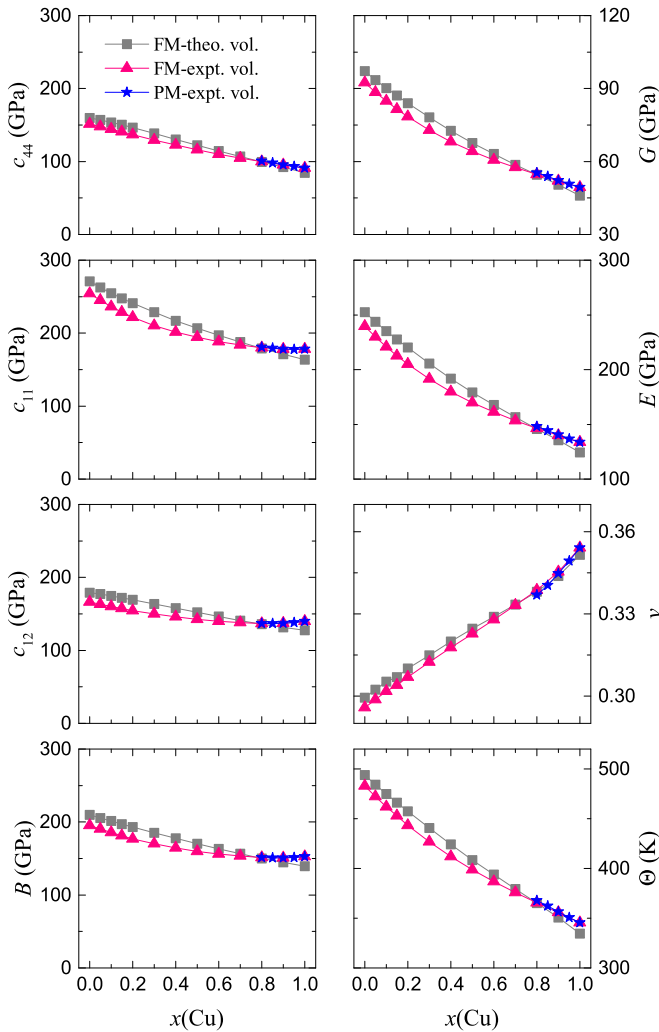


FIG. 4. Calculated elastic parameters and Debye temperatures of random fcc Co-Cu alloys as a function of Cu concentration x . The squares and triangles are results obtained for the FM state using theoretical (static) and experimental (room-temperature) volumes, respectively. The stars are computed for the PM state using the experimental volumes.

when using the experimental volume extrapolated to 0 K. However, adopting the volume at 1400 K leads to substantially larger T_C (close to 1600 K).

C. Elastic properties

Using the theoretical equilibrium (static conditions) and the experimental (room-temperature) lattice constants, we calculated the single and polycrystalline elastic parameters as well as the polycrystalline Debye temperature of Co-Cu random alloys. The results are plotted in Fig. 4 as a function of Cu concentration. We notice that the difference between the two sets of *ab initio* elastic constants does not fully reflect the effect of temperature (within the quasiharmonic approximation) when going from 0 K to room temperature since the theoretical equilibrium volumes and the estimated 0 K experimental volumes slightly differ (see, e.g., inset in Fig. 3). We will come back to this question later.

The single-crystal elastic constants calculated using the theoretical lattice parameters follow a nearly linear trend, whereas those calculated using the experimental lattice constants show a noticeable nonlinear behavior. For the polycrystalline elastic moduli and Debye temperature, the trends obtained when using the theoretical and experimental lattice parameters are similar to those found for the single-crystal elastic constants, and the results calculated using the experimental volumes show again a clear nonlinear trend. Furthermore, comparing the elastic constants and Debye temperatures obtained for the FM and PM states (using the experimental volumes), we find that the values and trends in these two sets of theoretical data are relatively close to each other suggesting that the direct magnetic contributions in these parameters are small.

In order to reveal the deviations relative to the linear trends, we introduce the following quantity [72]:

$$\Delta C(x) = C(x) - (1-x)C(0) - xC(1), \quad (2)$$

where $C(x)$ stands for a certain equilibrium property calculated for alloy with concentration x . By separating the nonlinear contribution $\Delta C(x)$, we can have a closer look and a more detailed investigation of the alloying effects.

The obtained nonlinear contribution for the elastic parameters are plotted in Fig. 5. All single-crystal elastic constants in Fig. 5 (left panels) strongly deviate from the linear behavior. The Δc_{ij} and ΔB calculated using the experimental volume follow a parabolic trend with the minimum appearing at 40–60% Cu and dropping by about 5–23 GPa. In the calculations using the static theoretical volume, Δc_{44} and Δc_{12} also show complex trends which differ from the parabolic trends of Δc_{11} and ΔB . Namely, Δc_{44} and Δc_{12} change sign at 60% and 30% Cu, respectively, while Δc_{44} has a blurred local maximum around 90% Cu concentration. Due to the nonlinear behaviors of the single-crystal elastic constants, the deviation of the polycrystalline elastic constants and Debye temperature shown in Fig. 5 (right panels) are expected to show also nonlinear behavior. Basically, the smooth curves similar to a parabolic trend are maintained for ΔG and ΔE calculated using the theoretical and experimental volumes. However, the Poisson ratio $\Delta \nu$ displays a complex curve with a maximum at 10% Cu. We notice that the complex composition dependences of c_{12} and c_{44} show good correlation with the trend of the adopted lattice parameters. Considering a regular volume dependence (i.e., elastic constant decreases with increasing volume), one finds that the trends of Δc_{12} and Δc_{44} for both experimental and theoretical volumes reflect well the trends of the corresponding lattice parameters in the inset of Fig. 2. In the case of c_{11} , the deviation compared to the linear trend is much larger than those obtained for c_{12} and c_{44} and resembles the one followed by B .

The calculated Debye temperature exhibits a similar trend as that of ΔG and ΔE . The minimum of ΔG , ΔE , and Debye temperature are close to 40% Cu, and that of $\Delta \nu$ to 80%. We notice that the strong negative deviation of the Debye temperature relative to the linear trend is critical for a positive excess entropy. This is because at high temperature the entropy is proportional to $S_{\text{vib}} = k_B[4 + 3\ln(T/\Theta)]$ [73], meaning that for instance for the equiatomic alloy $\Theta(0.5)$ should be below $\sqrt{\Theta_{\text{Co}}\Theta_{\text{Cu}}}$ in order to yield positive ΔS_{vib} .

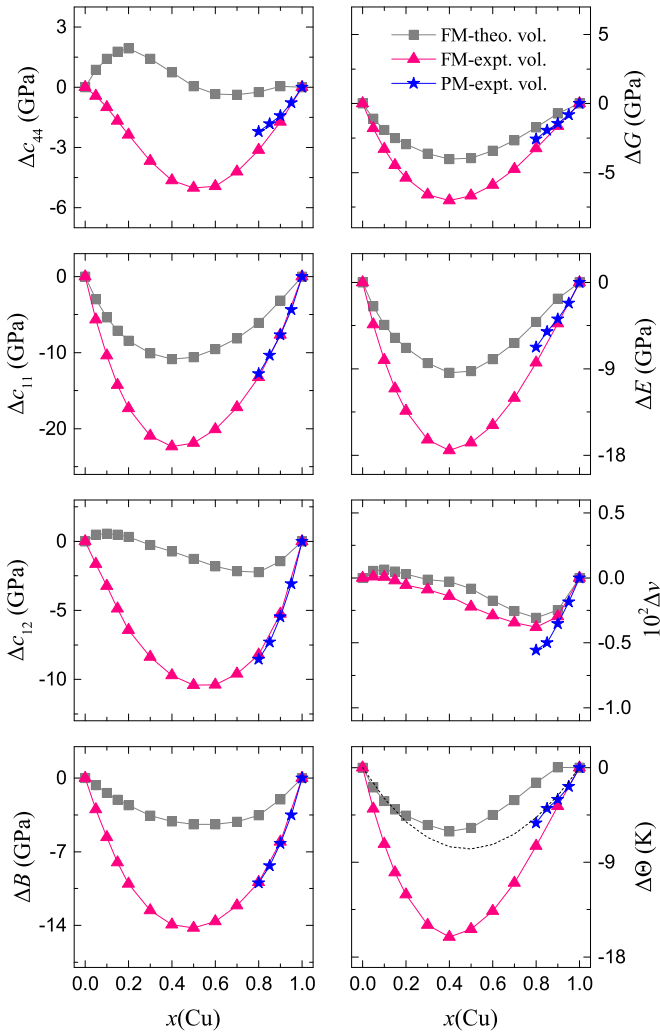


FIG. 5. Deviations from the linear behavior of the calculated elastic parameters and Debye temperature of random fcc Co-Cu alloys as a function of Cu concentration x . The squares and triangles are results in the FM state using theoretical (static) and experimental (room-temperature) volumes, respectively. The stars are computed adopting the PM state and the experimental (room-temperature) volumes. The thin dashed line marks $\Delta(\Theta_{\text{Co}}^{1-x}\Theta_{\text{Cu}}^x)$.

In Fig. 5, we indicate the critical values $\Delta(\Theta_{\text{Co}}^{1-x}\Theta_{\text{Cu}}^x)$ by a thin dashed line. Notice that when $\Theta(x)$ is below this critical value, the excess vibrational entropy is positive. Comparing the present theoretical trends to the critical Debye temperatures as defined above indicates that the vibrational entropy contributions will have different signs when computed using the theoretical and experimental lattice parameters. We will return to this question when discussing the excess entropy.

As described above, the elastic parameters derived using the experimental (room-temperature) volumes in the FM and PM states always follow a similar trend. However, the FM results show a significant difference when considering the theoretical and the experimental volumes. Therefore, we conclude that the effect of volume on elastic properties of random fcc Co-Cu alloys is significant whereas the effect of the magnetic state in the Cu-rich alloys is minor.

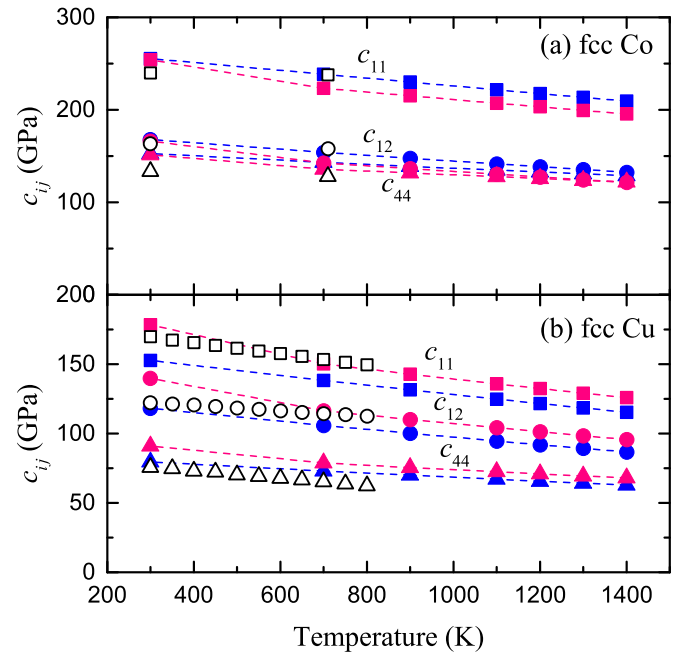


FIG. 6. Single elastic constants (c_{ij}) for fcc Co and Cu as a function of temperature. The solid symbols are the calculated elastic constants using the theoretical (blue) and experimental (pink) volumes as a function of temperature. The theoretical calculated c_{11} , c_{12} , and c_{44} are plotted as solid square, circle, and triangle, respectively. The available experimental data [74–76] (open symbols) are plotted for comparison.

So far we introduced results obtained for the theoretical (static) and experimental (room-temperature) volumes. However, for the phase diagram we need to have access to the temperature-dependent elastic parameters, i.e., we need to know the full $c_{ij}(T, x)$ functions. In Fig. 6, we present the calculated single elastic constants for pure Co and Cu as a function of temperature, together with the available experimental data [74–76]. The two sets of theoretical results were obtained using the theoretical volumes (theoretical equilibrium volumes scaled with the thermal expansion coefficient) and the experimental volumes (room-temperature experimental volumes scaled with the thermal expansion coefficient), respectively. Since we could not find experimental data for the alloys, the temperature dependence of the elastic constants for the alloys is not explicitly shown and discussed here. The theoretical (measured) c_{11} , c_{12} , and c_{44} are plotted as solid (open) square, circle, and triangle, respectively. In the case of fcc Co, the calculated elastic constants are in good agreement with the experimental values corresponding to room-temperature and 710 K. For fcc Cu, theory slightly overestimates c_{11} and c_{12} at low temperatures. In the case of c_{44} , the predicted temperature dependence follows closely the experimental trend. We also notice that the $c_{ij}(T, x)$ curves obtained for the theoretical and experimental volumes are very similar, although they are slightly shifted relative to each other due to the small differences between the theoretical and experimental volumes. In general, for the pure end members, the theoretical temperature factors reproduce the observed trends with high accuracy. Because the present theory is not limited

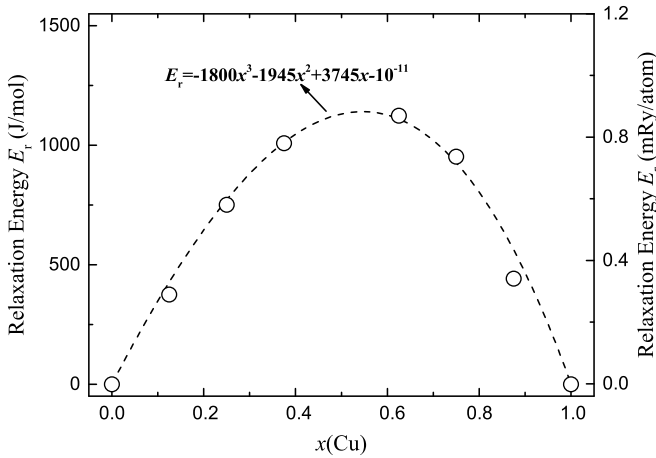


FIG. 7. Relaxation energy (E_r) as a function of the Cu concentration (x) for the Co-Cu alloys calculated using the GPAW-SQS method. The circles are the difference between the unrelaxed and relaxed energies for concentrations $x = 0.125, 0.25, 0.375, 0.625, 0.75, 0.875$. The dashed line is a polynomial fit of the E_r versus x dataset. Results are shown both in J/mol and mRy/atom units.

to the pure elements and there is no *a priori* reason why it should perform less accurately for solid solutions than for the elemental metals, we assume a similar level of accuracy for alloys as the one shown in Fig. 6. In the following, we use the so computed temperature and composition dependent elastic parameters to evaluate the thermodynamic quantities entering the Gibbs energy (1).

D. Enthalpy of formation

The enthalpy of formation of an alloy is an excess energy due to the additional interaction present in the alloy compared to the end members. Therefore all effects which are present in the alloy but missing in the pure components are critical for a quantitative estimation of the formation enthalpy. When combining elements with sizable differences in atomic volumes a significant local lattice distortion can develop. Since no atomic forces can be computed using the EMTO method, the local relaxation around individual atoms cannot be accounted for by this approach. Previous studies demonstrated that the relaxation energy within the EMTO-CPA scheme is in reasonable agreement with the one obtained in the PAW-SQS study. With the EMTO-CPA scheme, one can estimate the relaxation effect on the formation enthalpy using the effective tetrahedron approach developed by Ruban *et al.* [77]. This approach was found to perform well for a Cu-Au binary system [7]. Here we follow a different route and address the local lattice relaxation and the associated relaxation energy (E_r) in fcc Co-Cu alloys by using the GPAW method. As described in Sec. IIE, all atomic relaxation energies for Cu concentrations x were calculated in the FM state using the SQS scheme. All GPAW-SQS calculations were based on the corresponding theoretical equilibrium volume which are very close to those computed using the EMTO-CPA approach (see Fig. 2). The results are presented in Fig. 7. We find that the energy change due to the local lattice relaxation increases with Cu content,

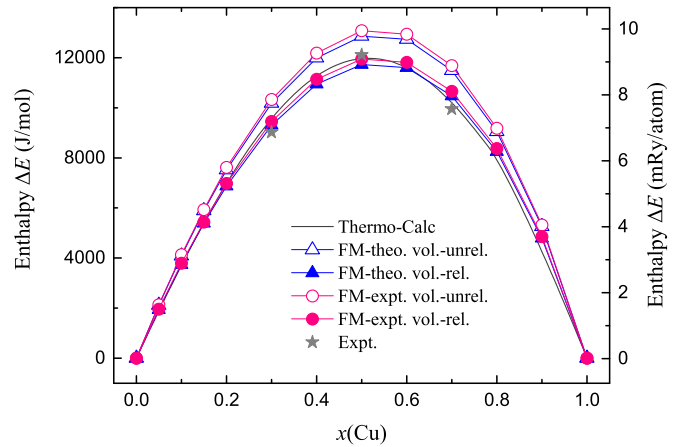


FIG. 8. Comparison between *ab initio* (unrelaxed and relaxed), Thermo-Calc, and experimental formation enthalpies for the Co-Cu system as a function of Cu concentration. All shown data correspond to room temperature, and the *ab initio* calculations were carried out using the room-temperature experimental volumes and for the FM state. The unrelaxed results are derived from the EMTO-CPA total energies, whereas the relaxed results take into account the relaxation energy shown in Fig. 7.

reaches a maximum of about 1172 J/mol around 55% Cu, and decreases in the Cu-rich side of the binary system. We fit the individual energies by a third-order polynomial function which will be used to correct the total energy and enthalpy obtained within the mean-field approximation. We notice that the same relaxation energy obtained for the FM state will be adopted for both FM and PM CPA results, i.e., we assume that in the Cu-rich end of the phase diagram the relaxation energy weakly depends on the magnetic state. One argument behind this assumption is that we see a relatively weak magnetic state dependence of the elastic properties in the Cu-rich alloys (Figs. 4 and 5).

The present *ab initio* results for the room-temperature formation enthalpy are shown in Fig. 8 as a function of Cu concentration. For comparison, we also show the Thermo-Calc results at room temperature and the available experimental data. All theoretical results correspond to the room-temperature volumes and to the FM state. It can be seen that the Thermo-Calc formation enthalpy is in good agreement with the experimental values [23], and the maximum value is around 12 kJ/mol. Both for the theoretical and experimental volumes, the calculated formation enthalpy without the local relaxation is higher than the Thermo-Calc and experimental data. However, when the local relaxation energy is included, the so-called relaxed formation enthalpy values are significantly reduced and come in an excellent agreement with the Thermo-Calc values, especially in Co-rich and Cu-rich regions. In general, comparing the results with and without relaxation, it can be concluded that the local relaxations are important for calculating the formation enthalpy of Co-Cu alloys.

Before ending this section, we notice that ordering could further affect the formation enthalpy of the binary alloy. Using the quasicrystalline structures considered for assessing the effect of short-range order on the lattice parameter, we estimated the

temperature where no sizable short-range order develops. We find that at temperatures above ~ 1300 K, the short-range order effects can safely be dropped. At temperatures around and higher than 1300 K, the configurational entropy term removes all ordering effects and the alloy is close to a fully random state. Therefore the theoretical formation enthalpy in Fig. 8 and in the following sections corresponds to fully random solid solutions. We notice that according to our calculations, below ~ 1300 K, short-range order effects could lower the Gibbs free energies and thus slightly affect the theoretical phase diagram. However, considering the experimental phase diagram these effects are expected to be minor.

E. Entropy

Within the present approximation, the vibrational and magnetic entropy contributions are decoupled and therefore they are computed separately. To compare the *ab initio* excess entropy to the Thermo-Calc value, we consider the sum of all entropies except the configuration entropy. We notice that the contribution of electronic entropy has been taken into account in electronic free energy (ΔF_{ele}) as shown in Eq. (1). Moreover, electronic entropy is rather small for the present binary system so one can safely ignore its effect in the excess entropy. Accordingly, in the FM state, the excess entropy is expressed as the vibrational entropy, $\Delta S_{\text{xs}}^{\text{FM}} = \Delta S_{\text{vib}}$, while in the PM state it consists of the vibrational and magnetic entropies, $\Delta S_{\text{xs}}^{\text{PM}} = \Delta S_{\text{vib}} + \Delta S_{\text{mag}}$. The calculated excess and total entropies corresponding to the room-temperature experimental volumes are plotted in Fig. 9 as a function of Cu concentration. For comparison, the entropy calculated by the Thermo-Calc software is also presented as well as the *ab initio* FM results obtained using the room-temperature theoretical volumes.

We notice that the present *ab initio* excess and total entropies using the experimental volume are in good agreement with the Thermo-Calc results. It is very important to observe that the agreement in the Cu-rich part is substantially improved when the PM state is considered and one accounts for the entropy due to the disordered magnetic state. The peculiar feature of the Thermo-Calc (in fact experimental) total entropy near 80% Cu can only be captured when one properly accounts for the magnetic state of Cu-rich alloys. This is because the magnetism of Cu-rich region of the Co-Cu alloys is correctly modeled as the paramagnetic state. Hence, the contribution of magnetic entropy in the Cu-rich region is not negligible and as we will see it below this term is the reason for the finite solubility of Co in fcc Cu at elevated temperatures. Compared to the PM results, the excess entropy calculated using the experimental volume and FM state in the Cu-rich region differs greatly from the experimental value. Finally we observe that calculations performed using the room-temperature theoretical volume lead to negative excess entropy within the Cu-rich region. It is mainly related to the calculated Debye temperature, which strongly depends on the adopted lattice parameters.

F. Free energy

First we present the *ab initio* free energies calculated using theoretical and experimental volumes at different

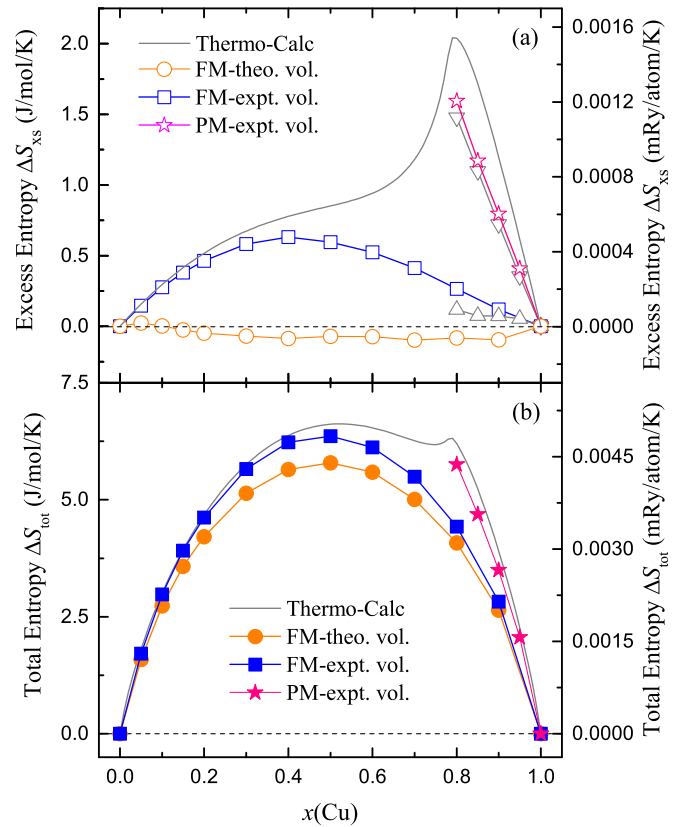


FIG. 9. Comparison between experimental (Thermo-Calc) and theoretical (present study) excess (ΔS_{xs}) and total (ΔS_{tot}) entropies for Co-Cu alloys plotted as a function of Cu concentration. In the upper panel, we also show the vibrational entropy (ΔS_{vib} , Δ) and magnetic entropy (ΔS_{mag} , ∇) obtained by using the experimental volumes in the PM state for reference. The shown data correspond to room temperature. For comparison we also give the theoretical results obtained for the FM state using the room-temperature theoretical volumes.

temperatures for fcc Co-Cu alloys within Co-rich and Cu-rich regions in Fig. 10. All shown results assume fully random solid solutions. For comparison, the Thermo-Calc free energies are also plotted as a function of Cu concentration x . For the Co-rich region in the FM state, the *ab initio* free energy has a reasonable agreement with the Thermo-Calc results. On the other hand, the calculated free energy of the Cu-rich region in the PM state is somewhat higher than the Thermo-Calc value, which is related to the slight underestimation (overestimation) of the total entropy (enthalpy) in this region, as shown in Fig. 9 (Fig. 8). Comparing the *ab initio* free energy using theoretical and experimental volumes, we find that the calculated free energy using experimental volumes have a better agreement with Thermo-Calc values. Based on the calculated free energies, the energy curves in Co-rich and Cu-rich regions at a given temperature share a common tangent line to obtain two concentration values, which define the phase boundaries in the calculation of phase diagram.

The so obtained results are collected and shown as circle and star symbols in Fig. 11. With increasing temperature, the free energy both of the Co-rich and Cu-rich region presents

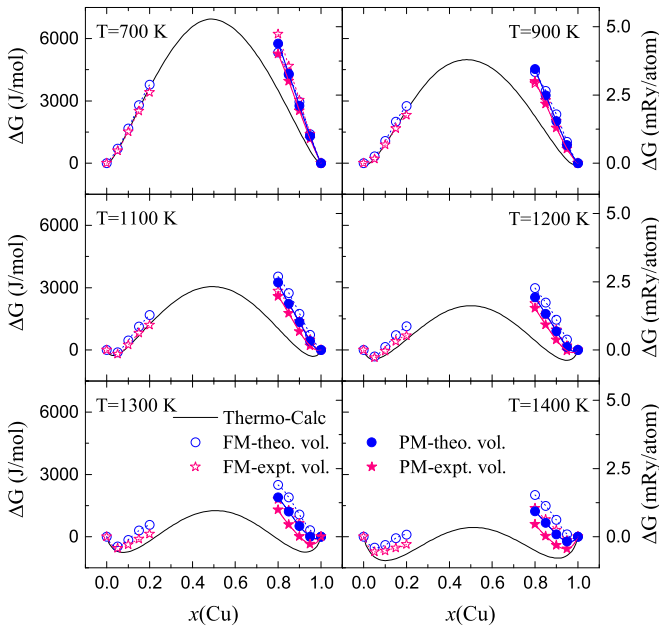


FIG. 10. Comparison between Thermo-Calc (solid lines) and *ab initio* (symbols) Gibbs free energy (ΔG) for Co-Cu alloys at different temperatures. The star (circle) symbols are the calculated Gibbs free energies using the experimental (theoretical) volumes as a function of Cu concentration x . We also show the FM results in the Cu-rich region for reference.

a more pronounced parabolic trend. The free energy trend in the Co-rich region (Cu concentration x from 0 to 0.2) is similar to the calculated phase diagram, and thus the phase diagram in this region is close to the Thermo-Calc result. However, in the Cu-rich region (Cu concentration x from 0.8 to 1), the

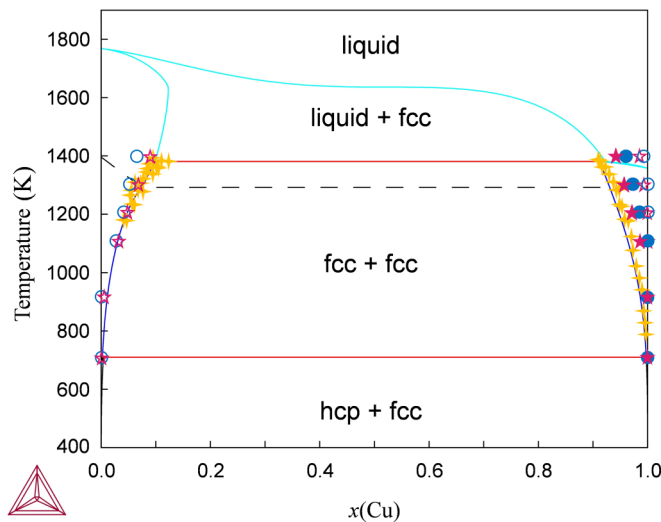


FIG. 11. Theoretical *ab initio* phase diagram (circles and stars) in comparison with the Thermo-Calc (solid lines) phase diagram, as well as the experimental values (cross symbols) [29,78–81]. The star (circle) symbols are the phase diagram predicted using the experimental (theoretical) volumes. The solid (open) symbols are the results in the PM (FM) state.

ab initio phase boundary somewhat deviates from the Thermo-Calc phase boundary but the trends are still very similar. For comparison, we also show the results in the FM state for using the experimental and theoretical volumes. It indicates that omitting the magnetic entropy removes the solubility in the Cu-rich side. In general, the phase diagram of Cu-Co alloys predicted using first-principles approach basically agrees with the Thermo-Calc results.

We briefly discuss the larger disagreement obtained for the Cu-rich alloys compared to the Co-rich alloys. As mentioned above, the deviation in the Gibbs free energies in Fig. 10 can primarily be ascribed to the smaller *ab initio* excess entropy than the Thermo-Calc value (Fig. 9). One could associate the missing excess entropy to clustering effects due to the different electronic structure of Co and Cu. However, since the difference between the *ab initio* and Thermo-Calc Gibbs energies for Cu-rich alloys in Fig. 10 is weakly temperature dependent, it is unlikely that this has a chemical ordering origin. Furthermore, according to our study, the chemical short-range order effects become negligible above 1300 K. Therefore, we rule out that clustering/ordering is the origin of the observed disagreement in Cu-rich alloys. Since the present magnetic entropy is a mean-field value (representing the upper limit of the paramagnetic entropy), we do not expect additional magnetic entropy effects either. Furthermore, we notice that the present theoretical vibrational entropy is based on the Debye model, which is known to have limited accuracy at temperatures far above the Debye temperature. Although our linear thermal expansion coefficient computed for Cu (not shown) follows closely the experimental trend even at the highest temperatures considered here [82,83], we cannot completely rule out that the vibrational entropy of Cu-rich alloys has reduced accuracy at high temperatures. On the other hand, we observe that the entropy for the Cu-rich alloys also depends on volume. Adopting theoretical or different sets of experimental volumes yields different excess entropy values for the Cu-rich alloys. Although this volume sensitivity seems a plausible explanation, further investigations are needed to find the exact origin of the obtained deviations.

IV. CONCLUSIONS

In the present work, we performed *ab initio* calculations in combination with alloy theory formulated within the EMTO-CPA approach to assess the phase diagram of Co-Cu alloys at temperatures 0–1400 K. Atomic relaxation was determined by a full-potential *ab initio* approach and was included in all calculations. The theoretical lattice constant results show a linear or even negative deviation compared to Vegard's law which is in sharp contrast to the experimental values having a clear positive deviation. This difference becomes critical in the calculations of the elastic parameters and derived thermophysical properties. The estimation of the Curie temperature indicates persisting magnetism in the Co-rich alloys and paramagnetism in the Cu-rich region. We calculated the vibrational entropy as a function of concentration using the theoretical and experimental volumes. The predicted excess entropy in Cu-rich region based on the theoretical volumes is negative, opposite to the Thermo-Calc value. When using the

experimental volume, the theoretical trends come in registry with the experimental trends. We show that the contribution of magnetic entropy to the free energy in the Co-Cu system is not negligible, which becomes evident by comparing the excess entropies of the Cu-rich region obtained for the FM and PM states and the one computed using the Thermo-Calc software. Basically, the phase diagram of Co-Cu alloys predicted by the present first-principles method has a good agreement with the thermodynamic and experimental data. The present systematic study of Co-Cu alloys not only provides an atomic-level understanding for predicting the phase diagram of Co-Cu system but also highlights the importance of high-temperature magnetism. Nevertheless, the positive deviation of the experimental data for the equilibrium volume compared to

Vegard's law remains an open question which calls for further investigations.

ACKNOWLEDGMENTS

We acknowledge the discussion with Dr. Anders Bergman. This work was supported by the Swedish Research Council (Grants No. 2015-5335 and No. 2017-06474), the Swedish Foundation for Strategic Research (Grants No. S14-0038 and No. SM16-0036), the Swedish Energy Agency, the Hungarian Scientific Research Fund (Grant No. OTKA 128229), the Chinese Scholarship Council, and the Carl Tryggers Foundation. The calculations were performed on resources provided by the Swedish National Infrastructure for Computing (SNIC) at the National Supercomputer Centre (NSC) in Linköping.

-
- [1] C. Wolverton, X. Y. Yan, R. Vijayaraghavan, and V. Ozoliņš, *Acta Mater.* **50**, 2187 (2002).
- [2] P. Rogl, R. Podloucky, and W. Wolf, *J. Phase Equilib. Diff.* **35**, 221 (2014).
- [3] S. Lu, J. Ågren, and L. Vitos, *Acta Mater.* **156**, 20 (2018).
- [4] H. L. Zhang, S. Lu, M. P. J. Punkkinen, Q. M. Hu, B. Johansson, and L. Vitos, *Phys. Rev. B* **82**, 132409 (2010).
- [5] Z. H. Dong, W. Li, S. Schönecker, S. Lu, D. F. Chen, and L. Vitos, *Phys. Rev. B* **92**, 224420 (2015).
- [6] S. Lu, *Acta Mater.* **111**, 56 (2016).
- [7] L. Y. Tian, L. H. Ye, Q. M. Hu, S. Lu, J. J. Zhao, and L. Vitos, *Comput. Mater. Sci.* **128**, 302 (2017).
- [8] Z. H. Dong, W. Li, D. F. Chen, S. Schönecker, M. J. Long, and L. Vitos, *Phys. Rev. B* **95**, 054426 (2017).
- [9] N. Saunders and A. P. Miodownik, *Calphad (Calculation of Phase Diagrams): A Comprehensive Guide* (Elsevier, Oxford, 1998).
- [10] H. Lukas, S. G. Fries, and B. Sundman, *Computational Thermodynamics: The Calphad Method* (Cambridge University Press, Cambridge, 2007).
- [11] A. R. Miedema, P. F. De Chatel, and F. R. De Boer, *Physica B+C* **100**, 1 (1980).
- [12] L. J. Gallego, J. A. Somoza, J. A. Alonso, and J. M. Lopez, *Phys. B: Condens. Matter* **154**, 82 (1988).
- [13] B. Sundman, B. Jansson, and J. O. Andersson, *CALPHAD* **9**, 153 (1985).
- [14] J. O. Andersson, T. Helander, L. Höglund, P. F. Shi, and B. Sundman, *CALPHAD* **26**, 273 (2002).
- [15] Thermo-calc documentation set, version 2020b, https://www.thermocalc.com/media/40962/thermo-calc_documentation-set.pdf (2020).
- [16] Q. Chen, K. S. Wu, G. Sterner, and P. Mason, *J. Mater. Eng. Perform.* **23**, 4193 (2014).
- [17] H. L. Chen, H. H. Mao, and Q. Chen, *Mater. Chem. Phys.* **210**, 279 (2018).
- [18] D. A. Andersson, P. A. Korzhavyi, and B. Johansson, *CALPHAD* **32**, 543 (2008).
- [19] L. J. Zhang, J. Wang, Y. Du, R. X. Hu, P. Nash, X. G. Lu, and C. Jiang, *Acta Mater.* **57**, 5324 (2009).
- [20] S. Bigdeli, H. Ehtehsami, Q. Chen, H. H. Mao, P. Korzhavyi, and M. Selleby, *Phys. Status Solidi B* **253**, 1830 (2016).
- [21] S. Kardellass, C. Servant, I. Drouelle, F. Z. Chrifi-Alaoui, M. Idbenali, A. Abahazem, A. Hidoussi, A. Bendarma, and N. Selhaoui, *Mater. Today Proc.* **24**, 140 (2020).
- [22] J. R. Davis, *Nickel, Cobalt, and their Alloys* (ASM International, Ohio, 2000).
- [23] C. Gente, M. Oehring, and R. Bormann, *Phys. Rev. B* **48**, 13244 (1993).
- [24] M. A. Turchanin and P. G. Agraval, *Powder Metall. Met. Ceram.* **46**, 77 (2007).
- [25] B. B. Straumal, S. G. Protasova, A. A. Mazilkin, O. A. Kogtenkova, L. Kurmanaeva, B. Baretzky, G. Schütz, A. Korneva, and P. Zięba, *Mater. Lett.* **98**, 217 (2013).
- [26] A. Bachmaier, M. Pfaff, M. Stolpe, H. Aboulfadl, and C. Motz, *Acta Mater.* **96**, 269 (2015).
- [27] A. Bachmaier, J. Schmauch, H. Aboulfadl, A. Verch, and C. Motz, *Acta Mater.* **115**, 333 (2016).
- [28] J. Wang, S.-H. Oh, and B.-J. Lee, *Comput. Mater. Sci.* **178**, 109627 (2020).
- [29] T. Nishizawa and K. Ishida, *Bull. Alloy Phase Diagrams* **5**, 161 (1984).
- [30] X. Fan, T. Mashimo, X. S. Huang, T. Kagayama, A. Chiba, K. Koyama, and M. Motokawa, *Phys. Rev. B* **69**, 094432 (2004).
- [31] P. Hohenberg and W. Kohn, *Phys. Rev.* **136**, B864 (1964).
- [32] L. Vitos, *Phys. Rev. B* **64**, 014107 (2001).
- [33] J. P. Perdew, K. Burke, and M. Ernzerhof, *Phys. Rev. Lett.* **77**, 3865 (1996).
- [34] H. Levämäki, M. P. J. Punkkinen, K. Kokko, and L. Vitos, *Phys. Rev. B* **86**, 201104(R) (2012).
- [35] H. Levämäki, M. P. J. Punkkinen, K. Kokko, and L. Vitos, *Phys. Rev. B* **89**, 115107 (2014).
- [36] H. Levämäki, M. Kuisma, and K. Kokko, *J. Chem. Phys.* **150**, 054101 (2019).
- [37] J. P. Perdew, A. Ruzsinszky, G. I. Csonka, O. A. Vydrov, G. E. Scuseria, L. A. Constantin, X. Zhou, and K. Burke, *Phys. Rev. Lett.* **100**, 136406 (2008).
- [38] R. Armiento and A. E. Mattsson, *Phys. Rev. B* **72**, 085108 (2005).
- [39] P. Soven, *Phys. Rev.* **156**, 809 (1967).
- [40] B. L. Gyorffy, *Phys. Rev. B* **5**, 2382 (1972).
- [41] B. L. Gyorffy, A. J. Pindor, J. Staunton, G. M. Stocks, and H. Winter, *J. Phys. F Met. Phys.* **15**, 1337 (1985).
- [42] W. Kohn and L. J. Sham, *Phys. Rev.* **140**, A1133 (1965).

- [43] L. Vitos, *Computational Quantum Mechanics for Materials Engineers: The Emt Method and Applications* (Springer Science & Business Media, London, 2007).
- [44] P. E. Turchi, A. Gonis, and L. Colombo, in *Tight-Binding Approach to Computational Materials Science, Symposium Held December 1-3, 1997, Boston, Massachusetts, USA*, Vol. 491 (Materials Research Society, Warrendale, 1998).
- [45] O. K. Andersen and T. Saha-Dasgupta, *Phys. Rev. B* **62**, R16219 (2000).
- [46] L. Vitos, I. A. Abrikosov, and B. Johansson, *Phys. Rev. Lett.* **87**, 156401 (2001).
- [47] P. Olsson, I. A. Abrikosov, L. Vitos, and J. Wallenius, *J. Nucl. Mater.* **321**, 84 (2003).
- [48] L. Vitos, P. A. Korzhavii, and B. Johansson, *Nat. Mater.* **2**, 25 (2003).
- [49] S. H. Wei, L. G. Ferreira, J. E. Bernard, and A. Zunger, *Phys. Rev. B* **42**, 9622 (1990).
- [50] A. Zunger, S. H. Wei, L. G. Ferreira, and J. E. Bernard, *Phys. Rev. Lett.* **65**, 353 (1990).
- [51] A. H. Larsen, M. Vanin, J. J. Mortensen, K. S. Thygesen, and K. W. Jacobsen, *Phys. Rev. B* **80**, 195112 (2009).
- [52] J. E. Enkovaara, C. Rostgaard, J. J. Mortensen, J. Z. Chen, M. Duřak, L. Ferrighi, J. Gavnholt, C. Glinsvad, V. Haikola, H. A. Hansen *et al.*, *J. Phys.: Condens. Matter.* **22**, 253202 (2010).
- [53] J. J. Mortensen, L. B. Hansen, and K. W. Jacobsen, *Phys. Rev. B* **71**, 035109 (2005).
- [54] V. L. Moruzzi, J. F. Janak, and K. Schwarz, *Phys. Rev. B* **37**, 790 (1988).
- [55] J. P. Perdew and A. Zunger, *Phys. Rev. B* **23**, 5048 (1981).
- [56] D. E. Gray, *American Institute of Physics Handbook* (McGraw-Hill, New York, 1972).
- [57] K. Kádás, L. Vitos, B. Johansson, and J. Kollár, *Phys. Rev. B* **75**, 035132 (2007).
- [58] P. A. Korzhavii, A. V. Ruban, I. A. Abrikosov, and H. L. Skriver, *Phys. Rev. B* **51**, 5773 (1995).
- [59] M. Palumbo, S. Curtotto, and L. Battezzati, *CALPHAD* **30**, 171 (2006).
- [60] R. Lizárraga, F. Pan, L. Bergqvist, E. Holmström, Z. Gercsi, and L. Vitos, *Sci. Rep.* **7**, 1 (2017).
- [61] J. von Pezold, A. Dick, M. Friák, and J. Neugebauer, *Phys. Rev. B* **81**, 094203 (2010).
- [62] H. J. Monkhorst and J. D. Pack, *Phys. Rev. B* **13**, 5188 (1976).
- [63] L. Y. Tian, H. Levämäki, M. Kuusma, K. Kokko, Á. Nagy, and L. Vitos, *Phys. Rev. B* **99**, 064202 (2019).
- [64] J. M. Cowley, *J. Appl. Phys.* **21**, 24 (1950).
- [65] M. Ropo, K. Kokko, and L. Vitos, *Phys. Rev. B* **77**, 195445 (2008).
- [66] L. Y. Tian, H. Levämäki, M. Ropo, K. Kokko, Á. Nagy, and L. Vitos, *Phys. Rev. Lett.* **117**, 066401 (2016).
- [67] J. Kübler, *Theory of Itinerant Electron Magnetism*, Vol. 106 (Oxford University Press, Oxford, 2017).
- [68] S. F. Matar, A. Houari, and M. A. Belkhir, *Phys. Rev. B* **75**, 245109 (2007).
- [69] K. Sato, L. Bergqvist, J. Kudrnovsky, P. H. Dederichs, O. Eriksson, I. Turek, B. Sanyal, G. Bouzerar, H. Katayama-Yoshida, V. A. Dinh *et al.*, *Rev. Mod. Phys.* **82**, 1633 (2010).
- [70] J. R. Childress and C. L. Chien, *Phys. Rev. B* **43**, 8089 (1991).
- [71] J. J. Host, J. A. Block, K. Parvin, V. P. Dravid, J. L. Alpers, T. Sezen, and R. LaDuca, *J. Appl. Phys.* **83**, 793 (1998).
- [72] E. K. Delczeg-Czirjak, L. Delczeg, M. Ropo, K. Kokko, M. P. J. Punkkinen, B. Johansson, and L. Vitos, *Phys. Rev. B* **79**, 085107 (2009).
- [73] G. Grimvall and D. Oberschmidt, *Int. J. Thermophys.* **20**, 353 (1999).
- [74] H. J. Leamy and H. Warlimont, *Phys. Status Solidi B* **37**, 523 (1970).
- [75] B. W. Bennett, Master's thesis, Michigan Technological University, 1979.
- [76] Y. A. Chang and L. Himmel, *J. Appl. Phys.* **37**, 3567 (1966).
- [77] A. V. Ruban, S. I. Simak, S. Shallock, and H. L. Skriver, *Phys. Rev. B* **67**, 214302 (2003).
- [78] A. Knappwost, *Z. Phys. Chem.* **12**, 30 (1957).
- [79] J. D. Livingston, *Trans. Metall. Soc. AIME* **215**, 566 (1959).
- [80] C. F. Old and C. W. Haworth, *J. Inst. Metals* **94**, 303 (1966).
- [81] M. Hasebe and T. Nishizawa, *CALPHAD* **4**, 83 (1980).
- [82] S. I. Novikova, *Thermal Expansion of Solids (in Russian)* (Nauka, Moscow, 1974).
- [83] D. V. Minakov and P. R. Levashov, *Phys. Rev. B* **92**, 224102 (2015).